ABSTRACT

BRYANT, SAMUEL TRENT. A Refined Quasi-Static Model of a Marine Tethered Coaxial Turbine (Under the direction of Dr. Matthew Bryant).

A contra-rotating turbine has two coaxial rotors, upstream and downstream, oriented to rotate in opposite directions. One rotor can be fixed to the stator of an onboard generator and the other to the generator rotor to produce a direct-drive electromechanical system. This configuration is attractive for its inherent passive torque cancellation, as the opposite rotation of the two rotors results in steady-state hydrodynamic rotor torques of opposite directions and equal magnitude. Instead of a gearbox or an active control system, the operating points of a contra-rotating turbine are determined by the electrical load applied to the onboard generator. The relative simplicity of this turbine configuration makes it an attractive option for far-offshore marine power generation, where tower-mounted turbines become difficult and expensive to implement. Prior work has predicted the performance of tethered marine contra-rotating turbines as a function of tip speed ratio, and the behavior of the turbine has been modeled with both a dynamic model and a simplified quasi-static model. This quasi-static model and the experimental campaign conducted to validate it are the basis of this study. This thesis proposes a more robust quasi-static model that relaxes several key assumptions of the existing simplified model, such as the behavior of the downstream rotor in the wake of the upstream rotor. This thesis also re-processes the data recorded during the prior study's experimental campaign to reflect the behavior of the experimental turbine more accurately. The refinements in both the model and data result in a marked improvement in the agreement between the two, such that the predictions are captured within the uncertainty inherent to the experimental results.

A Refined Quasi-Static Model of a Marine Tethered Coaxial Turbine

by
Samuel Bryant

A thesis submitted to the Graduate Faculty of
North Carolina State University
in partial fulfillment of the
requirements for the degree of
Master of Science

Mechanical Engineering

Raleigh, North Carolina
2023

APPROVED BY:

_____	_____
Dr. Matthew Bryant	Dr. Kenneth Granlund
_____	
Dr. Andre Mazzoleni	

BIOGRAPHY

Sam Bryant received attended Johnston Community College, where he received his associate degree in engineering in 2017. In 2019, he received his bachelor's degree in mechanical engineering from North Carolina State University while participating in undergraduate aeroelasticity research under NCSU's Intelligent Systems and Structures Research Lab (iSSRL), where he continued as a researcher for marine renewable energy during his graduate career. Now, he teaches Mechanical Engineering Technology at Wake Technical Community College.

ACKNOWLEDGMENTS

I'd like to thank the sponsors of this project for their funding of this research. This marine coaxial turbine was sponsored by the Coastal Studies Institute through their North Carolina Renewable Ocean Program. and the tow system for the experimental campaign was supported by the U.S. Department of Energy under the award "Device Design and Robust Periodic Motion Control of an Ocean Kite System for Hydrokinetic Energy Harvesting" (Award No. DE-EE0008635).

I'd like to thank Mikayla Nichols for providing the initial concept, modeling, and experimentation of this project, as well as Vinson Williams for his assistance in developing and debugging the revised model used in this analysis. I'd also like to thank the rest of the students in iSSRL for all their encouragement and camaraderie, regardless of season.

I'd like to thank my advisor, Dr. Matthew Bryant, for the academic guidance I've received throughout my academic career, and for being an excellent example to strive for as a new teacher. Working as a researcher in iSSRL has taught me some of the most valuable lessons in presenting ideas to others.

Finally, I'd like to thank the rest of my committee, Dr. Kenneth Granlund and Dr. Andre Mazzoleni, for their advice and direction throughout the storied history of this research.

TABLE OF CONTENTS

LIST OF TABLES

LIST OF FIGURES

1. Introduction

Ocean currents are an attractive source of renewable offshore energy, but harvesting that energy comes with unique challenges. The Gulf Stream, for instance, passes by North Carolina, but as far as 100 km away from Cape Hatteras [1]. Additionally, the high-velocity flow environments most suitable for energy extraction are located as high as 3000m above the seafloor, and this high-velocity region does not have a constant location from year to year. These factors pose challenges for a traditional tower-mounted hydrokinetic turbine.

At sites like these, a tethered energy-harvesting system is a potential alternative. A tethered mooring system is more cost-effective at the scales required at such depths, and a tethered turbine could passively drift with the non-uniform current. However, since a hydrokinetic turbine transforms linear momentum from the ambient flow into angular momentum in one or more rotors, the turbine must be configured to avoid transmitting torque to the tether and prevent tether entanglement.

One potential solution is for the turbine to operate in zero net torque by extracting power with a pair of rotors operating in opposite directions. If the hydrodynamic torque from each rotor is of equal magnitude and opposite direction, then the net torque on the turbine is zero and the turbine can be attached to the tether by a simple swivel mount. The simplest configuration of this type of turbine is the direct-drive configuration, where an upstream and downstream rotor are each fixed to the rotor and stator of an onboard generator.

The first field-tested turbine of this configuration was developed by Clarke et al. at the University of Strathclyde [2]. This study established the direct-drive marine turbine as a proof-of-concept, and analysis was performed on modeling power generation as a function of tip speed ratio. Metoyer et al. studied a smaller-scale turbine, mounted in a water channel at North

Carolina State University, to determine how the steady-state operation of a direct-drive turbine was affected by skew angle [3]. Metoyer et al. also developed the first dynamic model for this turbine configuration to predict the behavior and operating points of a tethered marine turbine [4]. Another prototype was developed and tested by Nichols [5], who developed a simplified quasi-static model to predict the steady-state behavior of the experimental turbine.

This simplified model analyzes the rotors using blade element momentum theory (BEMT) to determine the relationship between flow speed, rotor speed, and rotor torque, and statically solves for a rotor-speed pair that yields a torque of equal magnitude, even with the reduced flow to the downstream, rotor. However, this simplified model is derived with several assumptions, such as the downstream rotor operating in the fully developed wake of the upstream rotor, as well as assumptions about the behavior of the rotor blades operating close to stall conditions.

This study proposes a refined quasi-static model that relaxes several of the assumptions made in the simplified model to more accurately capture the steady state behavior of the rotor and improve the agreement between the model predictions and experimental data presented in [5], as well as improve the processing of the data recorded during the experimental campaigns of that study.

2. Background

Direct-drive coaxial turbine

A direct-drive contra-rotating turbine has two bodies: one body houses the upstream rotor and the rotor of an onboard generator, and the other body houses the downstream rotor and the generator's stator. The rotor blades are oriented to facilitate the rotation of each body in opposite

directions via hydrodynamic torque. Additionally, the generator coupling between the upstream and downstream bodies also provides a source of torque and allows the bodies to react to each other. This turbine configuration is illustrated in Figure 1.

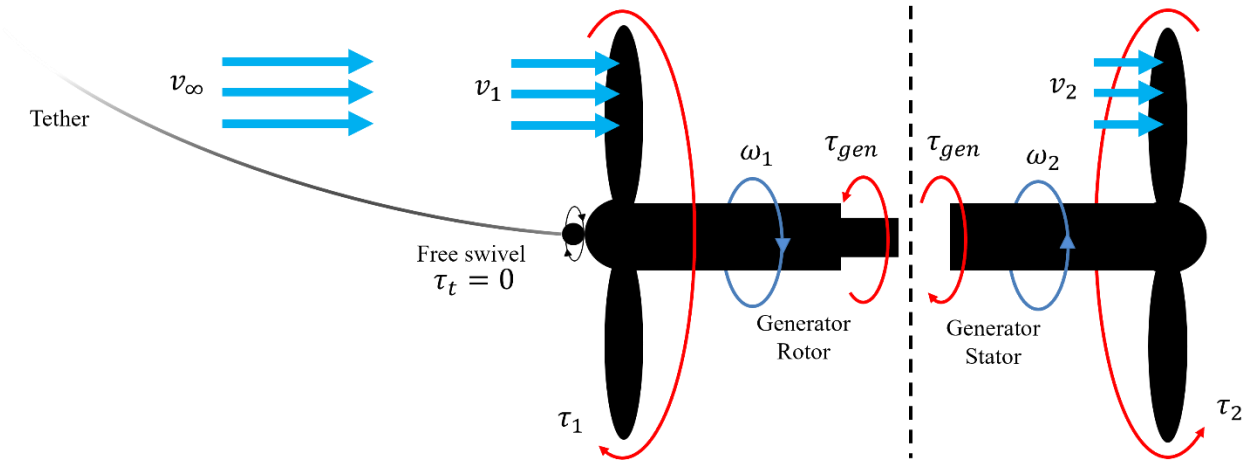

Figure 1. Torque and rotation of the upstream and downstream bodies in a contra-rotating turbine. This model does not account for mechanical losses like friction in the coupling. v_∞, v_1, and v_2 are the flow speeds at the far upstream, upstream rotor, and downstream rotor respectively, τ_t, τ_{gen}, τ_1, and τ_2 are torques produced by the tether attachment, generator, rotors respectively, and ω_1 and ω_2 are the angular rates of the rotors.

Since the turbine is fixed to a tether via a swivel, torque is unable to be mechanically transmitted away from the turbine. This means that barring mechanical losses like friction, the only moments acting on both the upstream and downstream rotors are the hydrodynamic torque from the flow acting on the rotor blades, as well as the generator coupling torque from the rotors acting on each other. For the turbine to operate in equilibrium, this means the hydrodynamic

torque at each blade must be of equal magnitude to the generator torque, forming the governing static equation of this turbine:

$$|\tau_1| = |\tau_2| = |\tau_{gen}| = \tau \tag{1}$$

This equality is referred to as "torque cancellation", and a direct-drive turbine allows this torque to be canceled passively. Hydrodynamic torque decreases with rotor speed, leading to a passive stability where any rotor that produces greater torque than the other will accelerate both rotors in the direction of that rotor, increasing the torque of the opposite rotor and decreasing its own torque. This is true even when the extraction of power from the surrounding flow by the upstream rotor causes a reduction in flow speed at the downstream rotor.

The differential rotation of these rotors allows for current to be generated via an onboard DC generator, as illustrated in Figure 2.

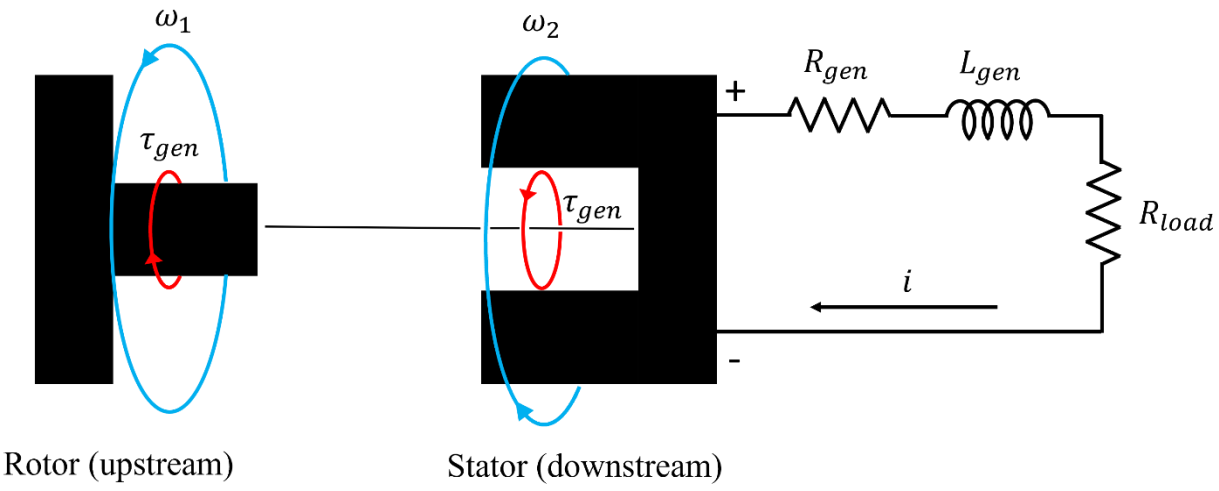

Figure 2. Circuit diagram of the onboard DC generator

Generators have two relationships to the current i produced by differential rotation, and these are governed by the voltage constant K_e and the torque constant K_τ inherent to the motor [6]. For an

ideal DC generator, these two constants are equal. The voltage produced by the generator can be written as

$$iR_{load} = -iR_{arm} + K_e(\omega_1 + \omega_2) \tag{2}$$

and the torque associated with that differential rotation can be expressed as

$$\tau = K_\tau i \tag{3}$$

Although generators have inherent induction L_{gen}, induction causes zero electrical impedance in a DC circuit, so it does not affect steady-state power generation.

Experimental prototype turbine

In the previous study presented by Nichols [5], a tow-test campaign was conducted for an experimental turbine. The characteristics of this turbine, shown in Figure 3, are presented here for clarity, as these turbine specifications are used for this study as well.

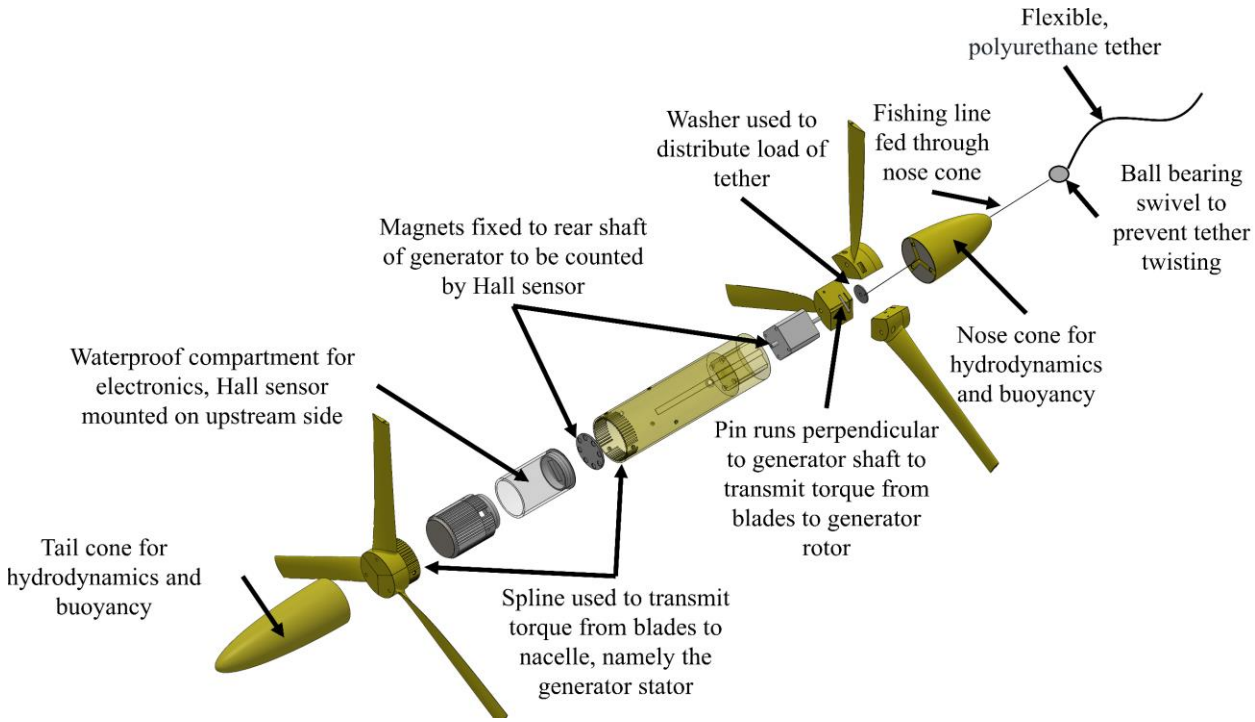

Figure 3. Exploded view of the experimental turbine.

Image credit: M. Nichols [5]

The body of the turbine is largely constructed from 3D-printed material, printed on a Stratasys Objet30. The rotor blades, nose cone, tail cone, and rotor nacelle were all manufactured using this method. The nose cone and tail cone are also filled with expanding polyurethane foam to facilitate buoyancy, and the turbine is weighted to operate as close to zero skew angle as possible. Nose to tail, the turbine is 62.5 cm long, and the nacelle has a diameter of 6.6 cm.

The rotor blades each have a diameter of 50 cm and are designed with a uniform chord of 3.125 cm and a uniform SG6040 airfoil, selected for its performance at low Reynolds numbers. These rotors are placed 25 cm apart, a distance equal to half the rotor diameter. The twist of the rotors is prescribed according to the design in [7].

For power generation, a MotionKing 17HS8401 stepper motor is used for the onboard generator. A brushless motor was chosen due to the marine environment, and a stepper motor

was chosen for its cost and ability to generate high voltage. The 17HS is a 2-phase stepper motor, but the current from each phase is bridged in a rectifier circuit and smoothed with a capacitor to achieve DC power generation. A resistor connects the terminals of this DC circuit to emulate an electrical load, such as a charging battery. The voltage constant of this motor was measured to be 0.423 V-s, and the internal resistance was measured to be 2.1Ω.

The turbine is also fitted with a suite of sensors to measure and record the mechanical data during an experiment. The downstream housing includes a Bosch BNO055 inertial measurement unit (IMU) to directly measure the rotation of the downstream rotor, and a Hall effect sensor is included to measure the differential rotor speed by counting the passes of eight small magnets fixed to the upstream housing. Both sensors are run by an onboard Arduino Uno microcontroller board, which reads the data from each sensor and records it to a microSD card. Additionally, the voltage across the terminals of the DC generator is measured by the Arduino's voltage sensor, and this voltage is used to calculate the generator current and torque according to (3).

This experimental turbine was observed in a tow-testing campaign, conducted in the pool at North Carolina State University's Casey Aquatic Center. The tow system consisted of a raft pulled across the diving well by a winch, and the tow speed of the raft could be prescribed, and this was used to emulate steady-state ambient flow for brief periods. The test apparatus was fixed to the underside of the raft by a tether connected to a sting roughly 2 meters below the surface of the water. This system is shown in Figure 4.

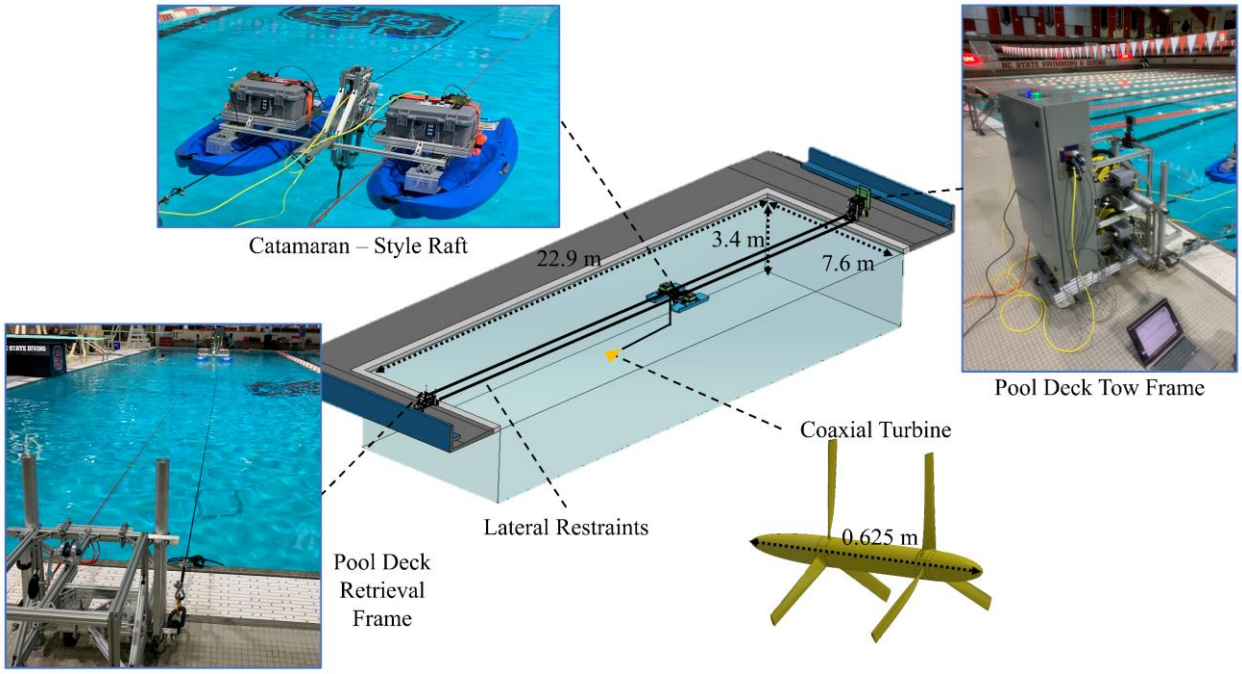

Figure 4. Experimental tow system for prescribing a flow speed $\boldsymbol{v}_\infty$

Image credit: M. Nichols [5]

The experimental campaign was run across a matrix of two experimental parameters: ambient flow speed and generator resistor load. The turbine was towed at four speeds, from 0.47 m/s to 0.77 m/s, and these tests were run with four different resistors, measured to be 250Ω, 515Ω, 752Ω, and 982Ω. These parameters yielded 16 tests, and the rotor speeds and torque were recorded over the duration of each. The downstream rotor speed for the tow tests conducted with the 982Ω resistor can are shown as an example in Figure 5.

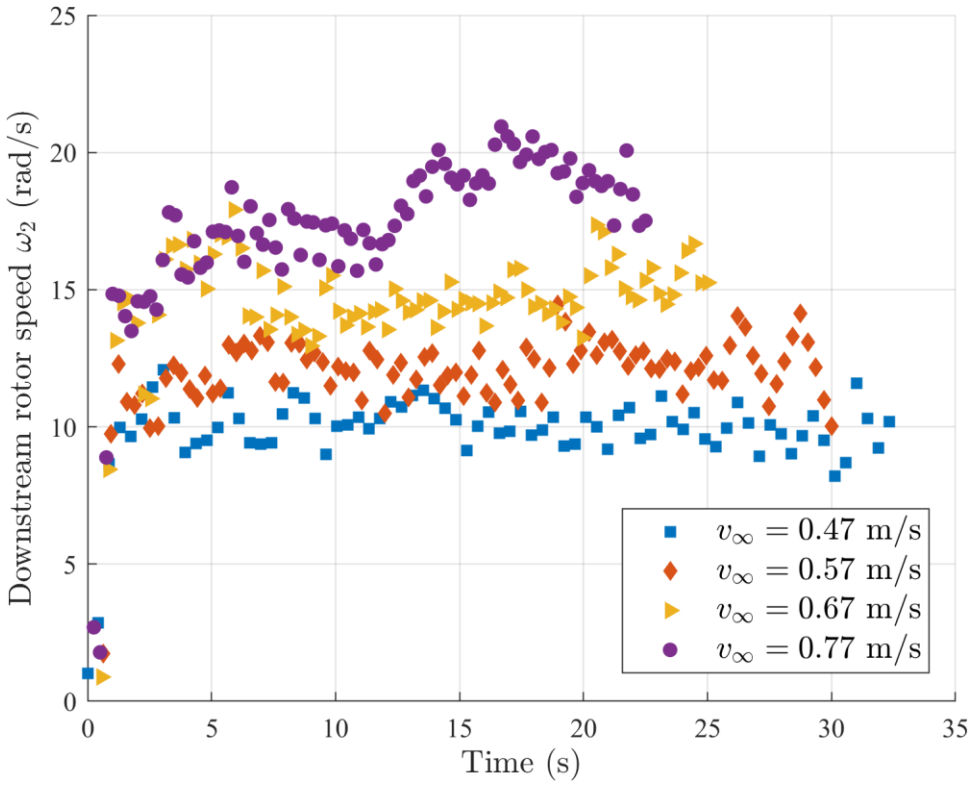

Figure 5. Downstream rotor speed recorded during four experimental runs at $\boldsymbol{R_{load}}$ = 982**Ω**. The steady-state assumption is verified by the trend of the data plateauing after initial transients.

At each time step, the downstream rotor speed was recorded, as well as the generator voltage, which was used to calculate upstream rotor speed via (2) and generator torque via (3) for that time step.

Predictions vs. measurements from Nichols' study

The data was collected over the 16 experimental runs, and the time-averaged values for upstream rotor speed, downstream rotor speed, and generator torque are presented. These experimental averages are compared with the steady-state predictions from the simplified quasi-static model and are plotted against experimental tow speed in Figure 6 - Figure 8. The plots are

also grouped according to the resistor fitted during each experiment. The error bars in the experimental results represent one standard deviation of the data collected over the associated run.

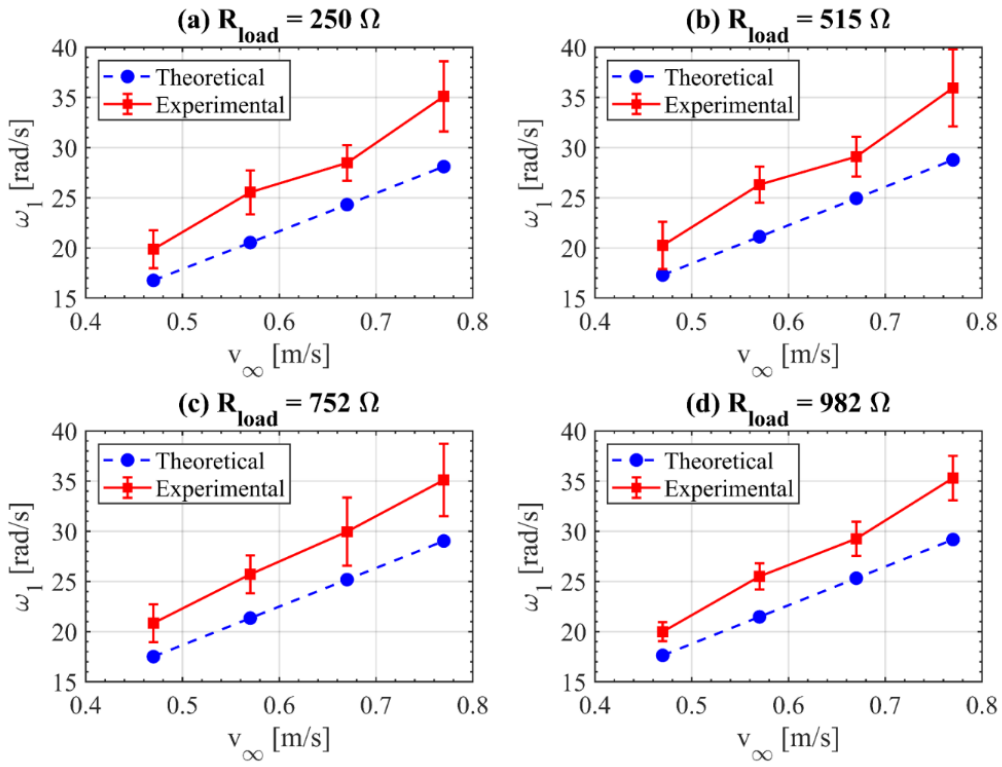

Figure 6. Model predictions vs. experimental results for steady-state upstream rotor speed. Error bars indicate one standard deviation of the measurements. Image credit: M. Nichols [5]

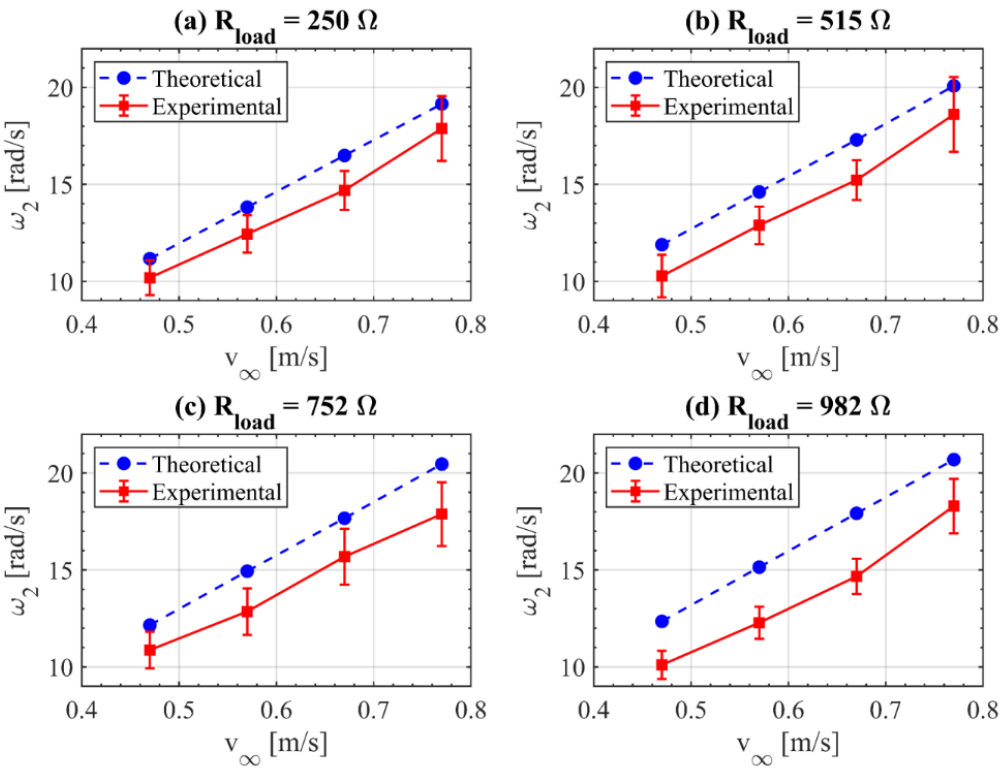

Figure 7. Model predictions vs. experimental results for steady-state downstream rotor speed. Error bars indicate one standard deviation of the measurements. Image credit: M. Nichols [5]

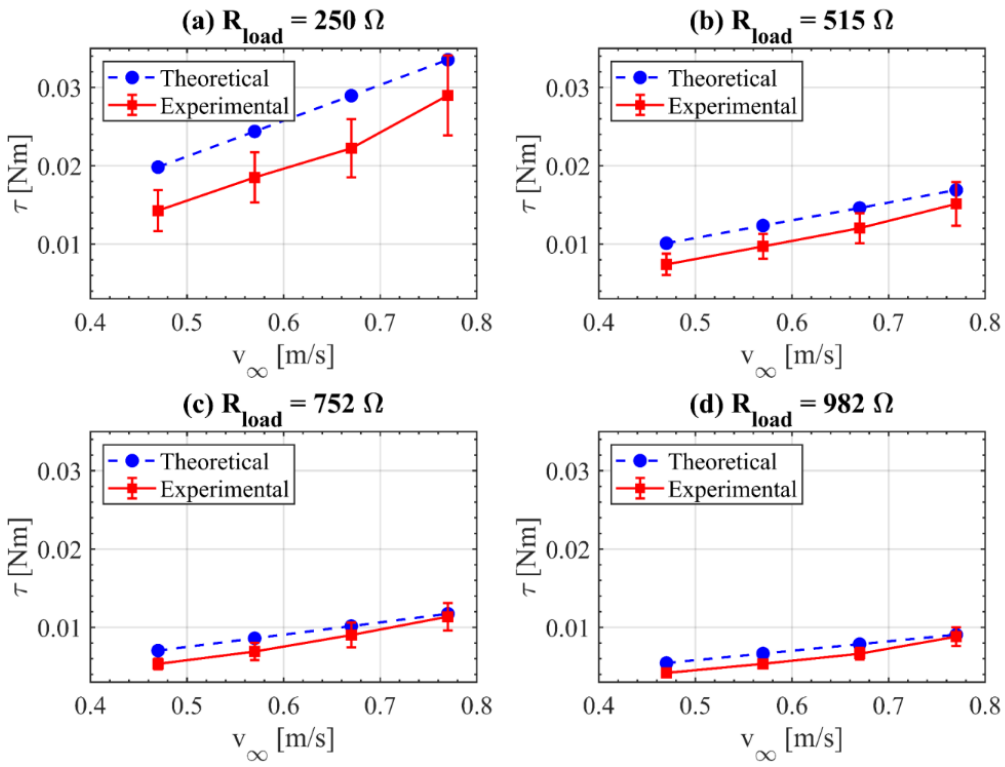

Figure 8. Model predictions vs. experimental results for steady-state turbine torque. Error bars indicate one standard deviation of the measurements. Image credit: M. Nichols [5]

In each of these plots, the trends show agreement between the model prediction and the experimental data. However, none of these figures show close agreement between the two, as the prediction is not captured within the uncertainty of the experimental recording.

According to these figures, three actions can be attempted to improve the agreement between the predictions and the experimental results. The first is that the data recorded during the experiment can be analyzed and reprocessed to ensure that it accurately represents the behavior shown during the experiment. The second is that the uncertainty associated with the experiment can be modeled and propagated to the results. Finally, improvements can be made to the quasi-static model to increase fidelity by more accurately capturing the hydrodynamic

behavior of the rotors. This study aims to accomplish all three, with the greatest emphasis on the third approach.

3. Refinement of Data Processing

Measurement of differential rotor speed

During the experimental campaign, the differential speed, as well as the upstream rotor speed by extension, were measured using the onboard Hall effect sensor. As the circularly spaced magnets passed in front of the sensor, the onboard processor was programmed to count the time for five magnet passes to occur. However, several issues were found in how this time was calculated.

First, due to an error in the code, the count always started with one magnet pass already "counted", and the time used to calculate the rotor speed was that for four magnet passes instead of five, causing an overprediction of differential rotor speed by 20%. Additionally, the program to begin counting the magnets was not triggered by a magnet pass but was instead initiated whenever the code was reached in the program, which would alternate between the code for recording the data and reporting the data. The condition for recording a magnet pass was a low reading from the sensor, under the condition that there was not a preceding low reading as well. This meant that if the code initiated while the sensor was giving a low reading, the code would not have recorded a low reading in a previous step and would incorrectly report another "magnet pass" on initialization, increasing the overprediction even further.

Because of these errors, and because of the uncertainty in the timing of when each data point was recorded, the measurements from the Hall effect sensor are unable to be used. Since the raw generator voltage was recorded during the experiment, this study uses (2) to determine

the differential speed instead. This is a useful method, as this voltage is also used in the calculation of the generator torque.

Uncertainty quantification

The uncertainty of the experimental campaign is quantified by considering the measurement uncertainty due to the resolution of each sensor and the parametric uncertainty of tow speed due to tether wrapping in the winch. The uncertainty associated with each experimental parameter or measurement was propagated, and the resulting experimental uncertainty is shown below in Table 1.

Table 1. Uncertainty analysis for each measurement and parameter in the experimental setup

Measurement/Parameter	Component	Component Uncertainty	M/P Uncertainty
Back rotor speed (ω_2)	IMU	14-bit resolution, 2000 deg/s max angular rate	$\pm$0.0021 rad/s
Torque (τ)	Voltage Sensor	10-bit resolution, $\pm$9.8 mV	$\pm$ 16 µN·m
Tow speed (v_∞)	Winch	$\pm$ 1 tether wrap, or ~8% of spool radius	$\pm$8% speed

Of the three values analyzed, the highest uncertainty was associated with the tow speed due to the change in effective spool radius with tether wrapping. Because this uncertainty is several orders of magnitude higher than that of the other values, the measurement uncertainty of the other values is assumed to be negligible. Since tow speed is a control variable and not a measurement, the uncertainty can be projected onto the model prediction by multiplying the error of the control variable by the linearized slope of any state x plotted against it. This is expressed below:

$$\delta_x \approx \delta_{v_\infty} \frac{dx}{dv_\infty} \tag{4}$$

where δ_{v_∞} is the uncertainty in the tow speed v_∞, and $\frac{dx}{dv_\infty}$ is the linearized slope of state x with respect to v_∞. This provides a confidence band around the model prediction based on the bounds of potential experimental tow speeds.

4. Simplified Turbine Model

The basis of both the simplified model in [5] and the refined turbine model proposed in this study is blade element momentum theory (BEMT). BEMT combines momentum theory and blade element theory to determine the relationships between rotor geometry, ambient flow speed, rotor angular speed, thrust, and torque. In both [5] and this study, the blade geometry and the ambient flow speeds are prescribed, so BEMT is specifically used here to relate rotor speed to hydrodynamic torque. The formulation for the BEMT analysis used in this study comes from [7] and [9].

Rotor thrust and torque via momentum theory

Momentum theory is an analysis of flow through a rotor that treats the rotor as an abstract actuator disc. This disc acts on the flow with a specific thrust and torque, and the resulting change in momentum can be seen in the difference in flow between the entry and exit of a "streamtube", or tube of streamlines, as seen in Figure 9.

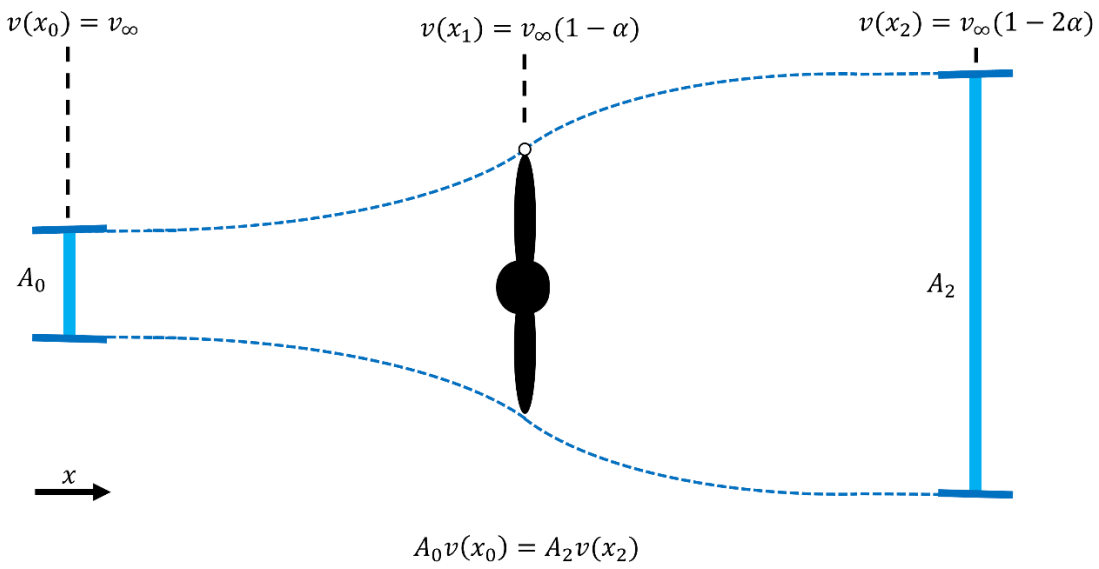

Figure 9. Streamtube defined by the actuator rotor disc.

According to the formulation detailed in [9], the degree to which the linear and angular momentum change in the flow from entry to exit of the streamtube can be expressed in terms of the axial and tangential induction factors a and a'. The effects of the axial induction factor on the velocity at the rotor and the far wake can be expressed as

$$v(x_1) = v_\infty(1-a) \tag{5}$$

$$v(x_2) = v_\infty(1-2a) \tag{6}$$

Analogously, the effects of the tangential induction factor can also be seen in the induced flow rotation ω_{flow} at the rotor and the far wake:

$$\omega_{flow}(x_1) = -\omega_{rotor}a' \tag{7}$$

$$\omega_{flow}(x_2) = -\omega_{rotor}2a' \tag{8}$$

In both sets of expressions, x_1 and x_2 are the positions of the actuator disc and the downstream rotor, respectively. Since these relations describe the flow local to the rotor disc, they can also be used to describe the apparent velocity seen by the rotor blades at the disc, as shown in Figure 10**.**

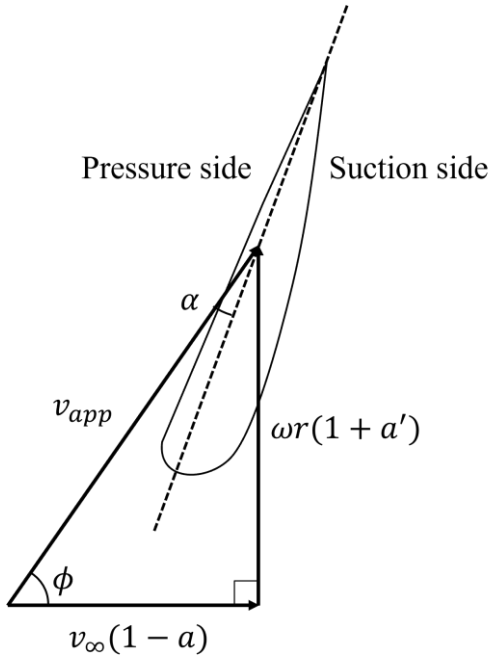

Figure 10. Local apparent velocity $\boldsymbol{v_{app}}$ at the rotor blade of an actuator disc.

The axial and tangential components to the apparent local velocity v_{app} can be expressed as

$$v_a = v_\infty(1-a) \tag{9}$$

$$v_t = r\omega(1+a') \tag{10}$$

where ω is the angular rate of the rotor blade.

Momentum theory also provides expressions for the resulting thrust and torque acting on the streamtube flow from the rotor disc and vice versa. For an ideal rotor disc, the thrust T and torque τ that acts on an annulus of a stream tube of radius R can be written as:

$$T = 2a(1-a)\rho v_\infty^2 \pi r^2 \tag{11}$$

$$\tau = a'(1-a)\rho v_\infty r^4 \omega \tag{12}$$

where ρ is the density of the fluid, v_∞ is the freestream velocity, r is the radius of the rotor disc, and ω is the angular speed of the rotor disc. BEMT discretizes the rotor into discrete blade elements, or annulus elements in an abstract rotor disc, so these expressions can be differentiated to obtain expressions for the annulus element dr:

$$dT = 4a(1-a)\rho v_\infty^2 \pi r dr \tag{13}$$

$$d\tau = 4a'(1-a)\rho v_\infty r^3 \omega dr \tag{14}$$

Although the derivation of momentum theory assumes the flow through the rotor disc is normal to the disc, flow near the tips of the rotor blades has an additional radial component, leading to lower projected velocity onto the rotor disc. To account for the reduced effects near the tip, the tip correction factor F_{tip} is introduced:

$$F = \frac{2}{\pi}\cos^{-1}(e^{-f}) \tag{15}$$

where e is Euler's constant, and

$$f = B\frac{r_{tip} - r}{2r\sin\phi} \tag{16}$$

Here, B is the number of blades in the rotor and ϕ is the angle of the inflow velocity with respect to the rotor plane as defined in Figure 10. The inflow angle ϕ can be derived from the velocity vectors shown in Figure 10:

$$\tan\phi = \frac{r\omega(1+a')}{v_\infty(1-a)} \tag{17}$$

This correction factor is implemented into the original thrust and torque equations:

$$dT = 4Fa(1-a)\rho v_\infty^2 \pi r dr \tag{18}$$

$$d\tau = 4Fa'(1-a)\rho v_\infty r^3 \omega dr \tag{19}$$

Rotor thrust and torque via blade element theory

Blade element theory analyzes the local interaction between the rotor blade and the surrounding fluid by discretizing the blade into smaller elements, each with its own airfoil and aerodynamic or hydrodynamic behavior. For a two-dimensional airfoil, the lift and drag of the fluid acting at a single blade element can be written as

$$dL = \frac{1}{2}\rho v_{app}^2 C_l(\alpha, Re) c dr \tag{20}$$

$$dD = \frac{1}{2}\rho v_{app}^2 C_d(\alpha, Re) c dr \tag{21}$$

where $\alpha = \phi - \beta$ is the local angle of attack, β is the local twist angle with respect to the rotor plane, Re is the local Reynolds number, c is the chord length of the element, and C_l and C_d are the Re-dependent airfoil lift and drag coefficients, obtained from a lookup table.

Since lift and drag are defined according to the direction of relative velocity, they are then resolved into normal and tangential forces according to the orientation of the rotor disc:

$$dF_n = dL\cos\phi + dD\sin\phi \tag{22}$$

$$dF_t = dL\sin\phi - dD\cos\phi \tag{23}$$

By introducing normal and tangential force coefficients C_n and C_t, these can be rewritten in the form of the original lift and drag equations as

$$dF_n = \frac{1}{2}\rho v_{app}^2 C_n(\alpha, Re) c dr \tag{24}$$

$$dF_t = \frac{1}{2}\rho v_{app}^2 C_t(\alpha, Re) c dr \tag{25}$$

where

$$C_n = C_l \cos\phi + C_d \sin\phi \tag{26}$$

$$C_t = C_l \sin\phi - C_d \cos\phi \tag{27}$$

With these forces expressed relative to the rotor disc, the incremental thrust and torque acting on the disc at each element can be written as

$$dT = dF_a B = \frac{1}{2} B\rho v_{app}^2 C_n c dr \tag{28}$$

$$d\tau = dF_a B r = \frac{1}{2} B\rho v_{app}^2 C_t c r dr \tag{29}$$

Blade element momentum theory (BEMT)

The solution for a given system is found at the intersection of momentum theory, which determines the flow's response to a prescribed rotor effect, and blade element theory, which determines the behavior at the rotor given local flow conditions. This intersection can be found by equating the expressions for thrust and torque found in (18) and (19) with those found in (28) and (29)

$$C_T \rho v_\infty^2 \pi r dr = \frac{1}{2} B \rho v_{app}^2 C_n c dr \tag{30}$$

$$4Fa'(1-a)\rho v_\infty r^3 \omega dr = \frac{1}{2} B \rho v_{app}^2 C_n c r dr \tag{31}$$

By defining disc solidity as $\sigma = \frac{cB}{2\pi r}$ and using the velocity relations shown in (17), these can be simplified to the following expressions:

$$C_T = C_n \sigma \frac{(1-a)^2}{\sin^2 \phi} \tag{32}$$

$$4Fa' = C_t \sigma \frac{(1+a')}{\sin \phi \cos \phi} \tag{33}$$

Alongside (17), these equations can be solved for the local values of a and a'. However, this dependency is highly nonlinear, so a and a' must be solved by using either iteration or optimization. This analysis solves for new values of a and a' with iteration, providing initial guesses for each, solving (17) for the inflow angle ϕ, then solving (32) and (33) for updated values of a and a':

$$a = \left(\frac{4F \sin^2 \phi}{\sigma C_n} + 1 \right)^{-1} \tag{34}$$

$$a' = \left(\frac{4F \sin \phi \cos \phi}{\sigma C_t} - 1 \right)^{-1} \tag{35}$$

This iterative process is complicated by the fact that the system can have multiple local extrema, as well as several singularities that the solver can get caught in. Many measures have been proposed for avoiding non-physical solutions and singularities by using both heuristic

measures and strategic choice of initial guesses, and the development of algorithms for solving the BEMT equations is an active field of research on its own [10][11][12].

When the new values of a and a' match the old values within the threshold $\varepsilon = 10^{-5}$, the system is solved, and (19) is used to calculate the blade element's incremental torque. The complete process for iteratively solving BEMT for a single disc element is summarized below:

1. Determine initial guesses for a_0 and $a_0{}'$. This analysis uses the values $a_0 = \frac{1}{3}$ and $a_0' = 2\left(\frac{3\omega r}{v_{in}}\right)^{-2}$.
2. For the k-th iteration, calculate new values of a_k and a_k' using the process below:
    a. From these values, calculate the inflow angle ϕ and the Reynolds number Re, as well as the resulting angle of attack α.
    b. Resolve the lift and drag coefficients into the normal and tangential coefficients C_n and C_t, and apply the tip loss corrections in (15).
    c. Calculate the new induction factors a_{new} and a'_{new} via (34) and (35).
3. If the values of a_{new} and a'_{new} do not match a_k and a_k' to within $\varepsilon = 10^{-5}$, update the induction factors $a_{k+1} = a_{new}$ and $a'_{k+1} = a'_{new}$ and repeat Step 2 until values match (convergence) or some maximum amount of iterations had been attempted (failure).
4. With the converged values of a and a', calculate incremental torque via (19).

This process is repeated at each element along the blade, and the incremental torque values are summed to determine the total torque acting on the rotor.

Dual-rotor analysis

To model the behavior of the downstream rotor, (6) is used to calculate the downstream flow velocity. With the downstream velocity known, the upstream and downstream rotors are analyzed in the same manner. To determine the rotor speeds where the upstream and downstream rotors produce torque equal to the torque produced by the generator, the rotors are analyzed simultaneously in an optimization loop, as detailed in Figure 11. Values are given for flow speed and resistive load across the generator, and MATLAB's **`fmincon.m`** function is used to minimize the difference in magnitude between the torque produced by the upstream and downstream rotors, subject to the constraint that both magnitudes are equal to that of the torque produced by the generator. The result of this optimization is a steady-state solution for upstream rotor speed ω_1, downstream rotor speed ω_2, and turbine torque $|\tau_1| = |\tau_2| = |\tau_{gen}| = \tau$.

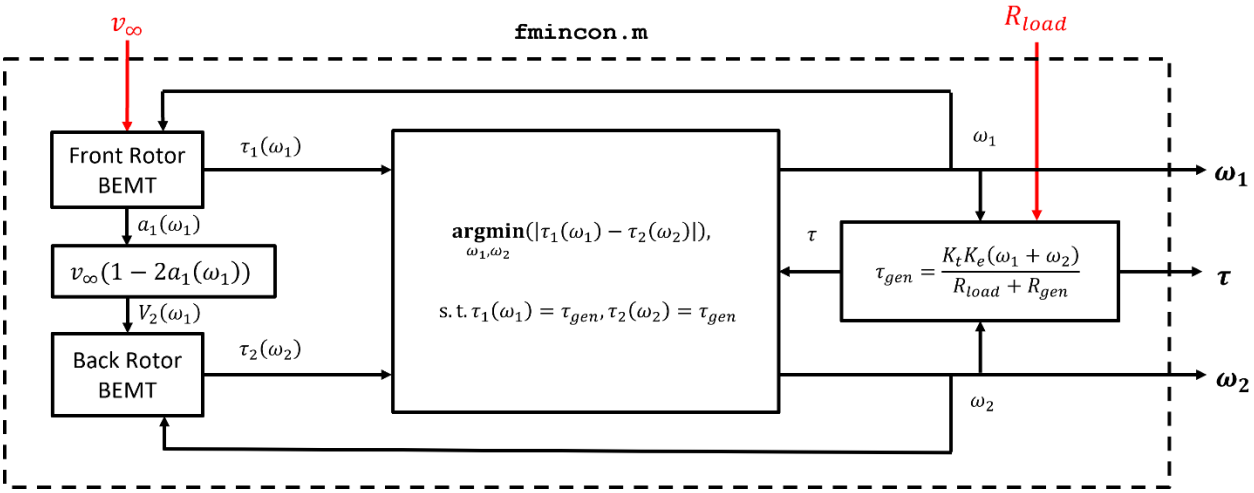

Figure 11. The solution method for the Nichols simplified turbine model

Assumptions of the simplified turbine model

The simplified turbine model operates with several assumptions inherent to its derivation as well as its solution method. One such assumption is the behavior of rotor elements with solutions of high induction factors. As suggested by (6), an axial induction factor higher than 0.5

would represent a fallacy where the flow would be reversed at the streamtube exit, violating conservation of mass for all nonzero flow speeds. The simplified model deals with this fallacy by ignoring all blade elements with solutions that contain $a > 0.5$ and extrapolating that those elements contribute incremental torque equal to the mean incremental torque of the remaining elements. This mean-value extrapolation is applied to the axial induction factor as well. The velocity expression in (6) also assumes that the downstream rotor operates in a fully developed wake. Neither the simplified model nor the refined model accounts for any mechanical losses in the turbine, such as friction, and both models assume one-way coupling of the flow from the upstream rotor to the downstream rotor, i.e., neglecting any effects of the downstream rotor on the upstream flow.

5. Model Refinements

Rotor behavior at high axial induction factors

This model relaxes the assumptions made by the simplified model of blade elements operating at high axial induction factors. Although classic momentum theory is not valid for high axial induction factors of $a > 0.5$, the behavior of rotors operating in such conditions is commonly modeled using an empirical relation [8],[9]. Rotors operating in the range of $0 < a < 0.5$ operate in the "windmill state", while rotors operating in the range of $0.5 < a < 1$ are in the "turbulent wake state". To model this behavior, the relationship between torque and the axial induction factor can be expressed as a piecewise function. To produce this expression, let the torque coefficient C_T can be defined as the following:

$$C_T = \frac{T}{\frac{1}{2}\rho v_\infty^2 A} = \frac{dT}{\frac{1}{2}\rho v_\infty^2 dA} \tag{36}$$

By combining (18) and (36), C_T for the "windmill state" is shown to be

$$C_T(a) = 4Fa(1-a) \tag{37}$$

The empirical relationship between C_T and a is accounted for by expressing $C_T(a)$ as a piecewise function, curve-fitting empirical data to produce a function for values up to $a = 1$. The function used in this analysis can be found in [8], and expresses C_T as

$$C_T(a) = \begin{cases} 4Fa(1-a) & , a \le a_c \\ 4F(a_c^2 + (1-2a_c)a) & , a > a_c \end{cases} \tag{38}$$

where the critical axial induction factor a_c has a given value of 0.2. With this new function, (18) can be written simply as

$$dT = C_T \rho v_\infty^2 \pi r dr \tag{39}$$

During the solution iteration of BEMT, if a is shown to have a higher value than a_c, then a is recalculated by the following expression:

$$a = \frac{1}{2}(2 + K(1-2a_c) - \sqrt{(K(1-2a_c)+2)^2 + 4(Ka_c^2 - 1)} \tag{40}$$

where

$$K = \frac{4F \sin^2 \phi}{\sigma C_n} \tag{41}$$

This updated value of a is used as the initial guess for the next iteration step in the BEMT solution process.

Additions to hydrodynamic modeling

Several changes are made from the simplified model regarding how the hydrodynamic behavior of the rotor blades is modeled. The simplified model uses experimental data for the lift and drag coefficients of the SG6040 airfoil [13], but the lookup table for this model does not include any dependency on the Reynolds number. This experimental lift and drag data are available for Reynolds numbers of 100,000 – 500,000, while the observed Reynolds numbers during the experimental campaign ranged from 50,000 to 150,000. Because a large portion of the analysis takes place below Re = 100,000, and because the lift and drag behavior of the airfoil changes significantly throughout the expected Re range as seen in Figure 12 and Figure 13, XFOIL is used to populate an Re-dependent lookup table for the BEMT model. This lookup table is also Re-dependent and is generated over the observed range of Reynolds numbers.

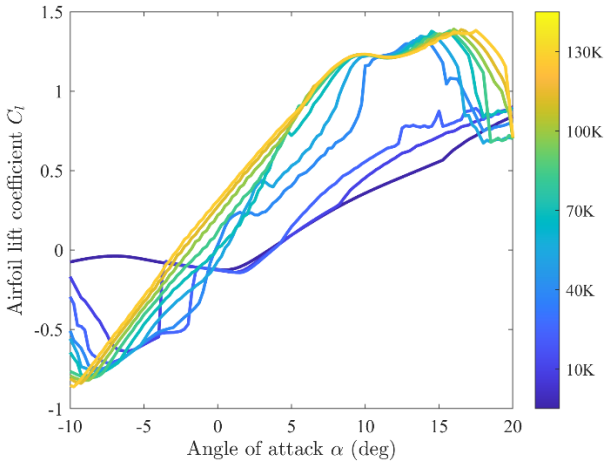

Figure 12. Sensitivity of the lift coefficient C_l to Reynolds number Re.

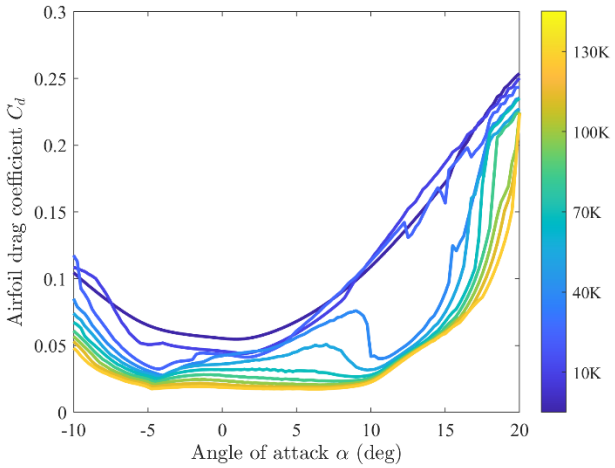

Figure 13. Sensitivity of the drag coefficient C_d to Reynolds number Re.

Another addition concerns the change in stall behavior due to the rotation of the rotor. Since the rotation of the rotor blade causes additional outward spanwise flow, stall occurs at a higher angle of attack than it would on non-rotating airfoil in steady flow, as modeled in [13]. This is modeled by adjusting C_l by the following expression:

$$C_{l,3D}(\alpha) = C_{l,2D}(\alpha) + 3\frac{c^2}{r^2}\Delta C_l(\alpha) \tag{42}$$

where

$$\Delta C_l(\alpha) = \frac{dC_l}{d\alpha}(\alpha - \alpha_0) - C_{l,2D}(\alpha) \tag{43}$$

Here, $C_{l,2D}$ is the lift coefficient obtained from the lookup table, $\frac{dC_l}{d\alpha}$ is the slope of the linear portion of the lift curve, a_0 is the zero-lift angle of attack, and ΔC_l is the lift deviation from the linear fit that widens after stall.

Heuristic methods added to BEMT solution process

Several heuristic measures are implemented in this analysis to improve the performance of the iterative solver. The first measure is a correction to the prediction of a and a', where a' can only be predicted to be a negative value if a is a negative value as well. This assumption is relaxed in the final performance calculation, as a' becomes negative before a near the rotor tip at high speeds, but the temporary constraint helps the solver avoid divergent or repeating iterations. Additionally, any element that fails to converge is compared with its converged neighbor, and BEMT is re-run using the converged values of a and a' as initial guesses. A relaxation factor of 25% is also introduced at this stage to scale the updates for a and a' with each BEMT iteration:

$$a_{k+1} = a_k + 0.25(a_{new} - a_k) \tag{44}$$

$$a'_{k+1} = a'_k + 0.25(a_{new} - a'_k) \tag{45}$$

Finally, if an element still fails to converge, which is more likely to occur when analyzing low flow speeds, the element is analyzed at several higher flow speeds until a cluster of solutions is found and a polynomial fit is used to extrapolate the solution at the lower flow speed.

Unknown downstream wake development

This model also relaxes the assumption that the downstream wake is fully developed at the location of the downstream rotor. The experimental tow-test campaign had no instrumentation to measure the local flow speed at each rotor, so there is no way to validate the assumption from the data recorded. Therefore, this study considers the lower and upper bounds of wake development at the downstream rotor. For an undeveloped wake, the flow entering the downstream rotor's streamtube is the velocity at the upstream rotor, but for a fully developed wake, this flow is the velocity of the upstream rotor's far downstream wake instead. This wake development can be generalized with the variable $\kappa(x)$. With this, (5) and (6) can be written as a single general expression:

$$v_{wake}(x) = v_\infty(1 - \kappa(x)a_1) \tag{46}$$

where the bounds of κ are $\kappa = 1$ for an undeveloped wake and $\kappa = 2$ for a fully developed wake. The effects of the downstream rotor operating at various degrees of wake development is illustrated in Figure 14.

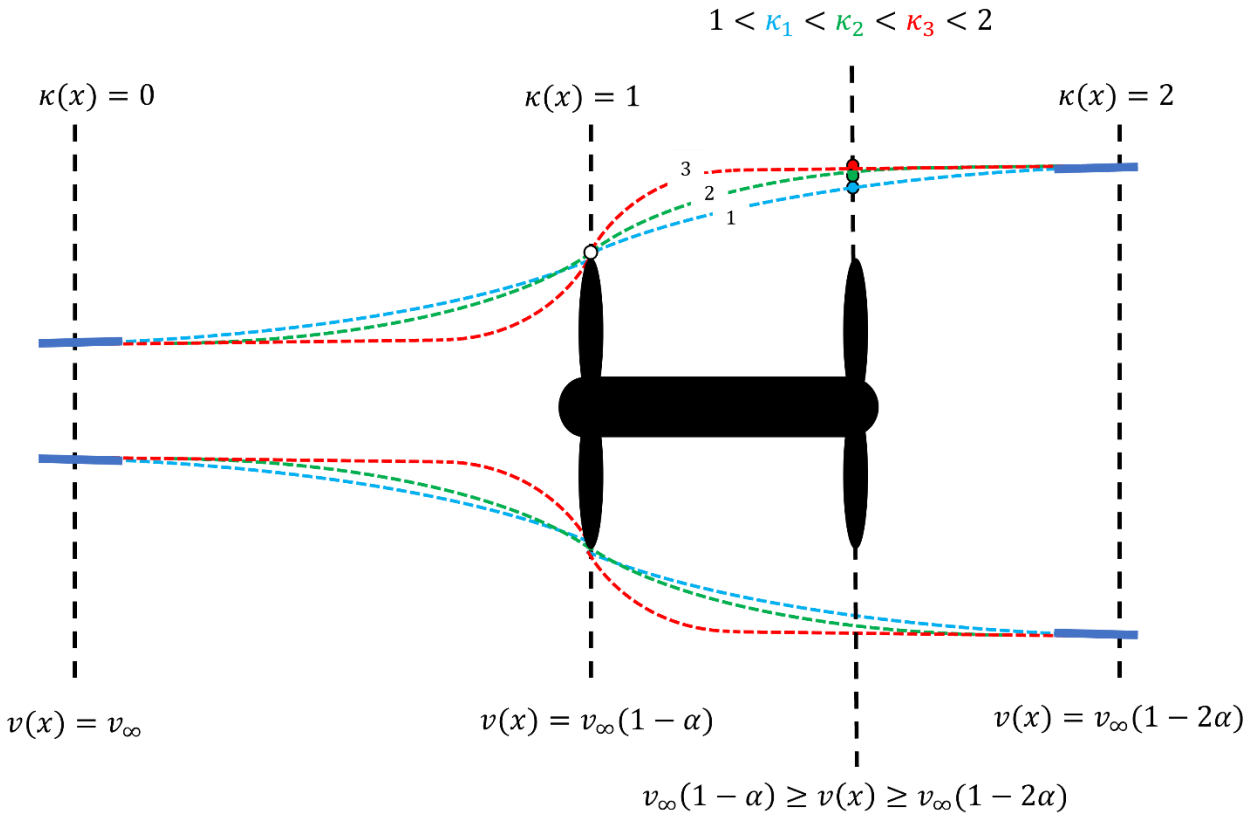

Figure 14. The effects of wake development speed on the flow speed at the downstream rotor

In this illustration, three different streamtubes of different wake development speeds, labeled 1, 2, and 3, are shown. All three have identical flow speeds and cross-sections at the streamtube entry, streamtube exit, and upstream rotor. However, in the regions between these points, the distance-dependent cross-sections and flow speeds are unknown. Streamtube "1" develops the most gradually and the associated $\kappa(x)$ value at the downstream rotor is the lowest of the three, so this streamtube would lead to the lowest cross-sectional area and the highest flow speed at the downstream rotor. The reverse is true for streamtube "3", the streamtube that develops the most quickly, and the associated downstream flow speed would be the lowest of the three.

Since the wake development was not observed during the pool-testing campaign, this study expands the analysis by modeling the turbine at several potential degrees of wake development, including the upper and lower bounds.

Proposed solution method for predicting operating points

This study proposes a new solution method for predicting the turbine's steady-state operating points, as illustrated in Figure 15. This solution method analyzes the rotors sequentially instead of simultaneously, and only the downstream rotor is modeled within an optimization loop. This model is prescribed a flow velocity v_∞ and an assumed downstream wake development factor $\kappa(x_2)$, and a 4-way locus of equilibria is calculated for upstream rotor speed ω_1, downstream rotor speed ω_2, turbine torque $|\tau_1| = |\tau_2| = |\tau_{gen}| = \tau$, and required resistive load R_{load}.

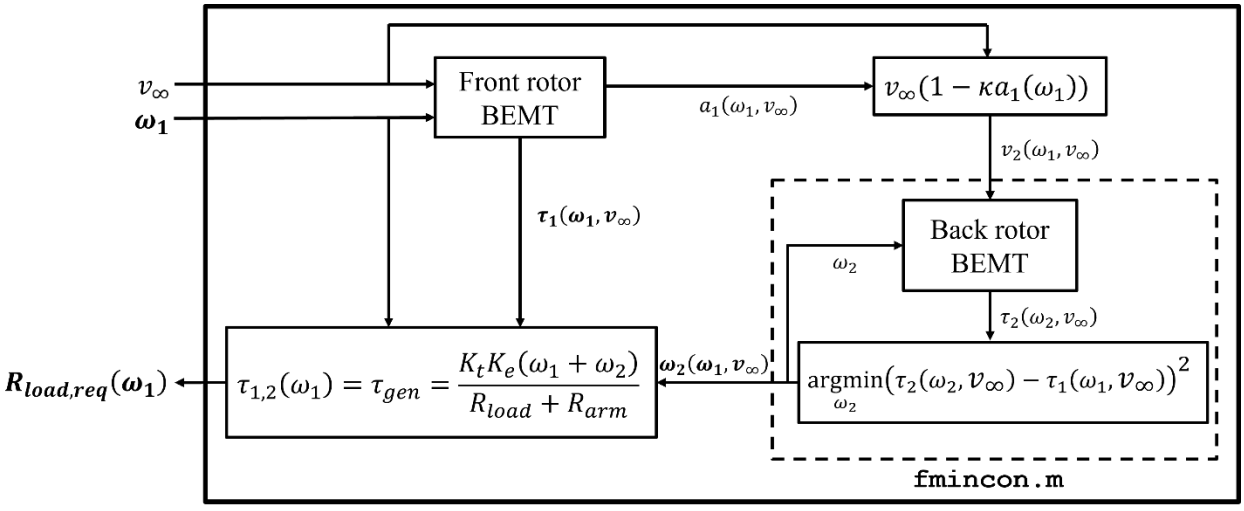

Figure 15. Sequential process for refined dual-rotor analysis

To begin the analysis, a range of ω_1 is specified, and BEMT is used to analyze the upstream rotor at each of these speeds to determine the resulting rotor torque $\tau_1(\omega_1)$. The analysis for the tow speed $v_\infty = 0.47$ m/s can be seen in Figure 16. Here, the minimum valid rotor speed $\omega_{1,min}$ represents the lowest rotor speed where at least one blade element has an angle of attack lower than 16°, the angle of expected stall [13], and the maximum valid rotor speed $\omega_{1,max}$ is the highest rotor speed with a non-negative hydrodynamic torque, as a negative torque would be indicative of the rotor driving the rotation of the flow instead of being driven. Additionally, the front rotor speed can be divided into an unstable range and a stable range, based on the slope of torque with respect to rotor speed. With a positive torque-speed slope, any increase in rotor speed also leads to increased torque, which again increases rotor speed, and so on, but with a negative torque-speed slope, an increase in rotor speed would decrease torque and cause the rotor to slow back down. This stable region provides a new, narrower range of front rotor speeds to feed forward into the analysis.

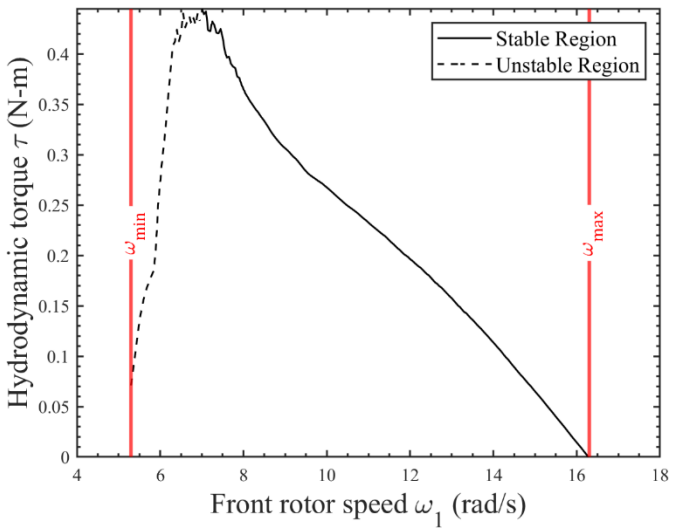

Figure 16. Upstream rotor torque as a function of upstream rotor speed, given am ambient flow speed of 0.47 m/s

The BEMT analysis of the front rotor also yields the upstream rotor's induction factor as a function of rotor speed. This can be used to populate a function for the downstream flow speed $v_2(\omega_1, \kappa)$ as well. Since the wake expansion factor is unknown, this analysis is performed at several possible degrees, where $\kappa = 1$ corresponds with the highest possible downstream rotor speed and $\kappa = 2$ with the lowest. The analysis for the $v_\infty = 0.47$ m/s case is shown in Figure 17.

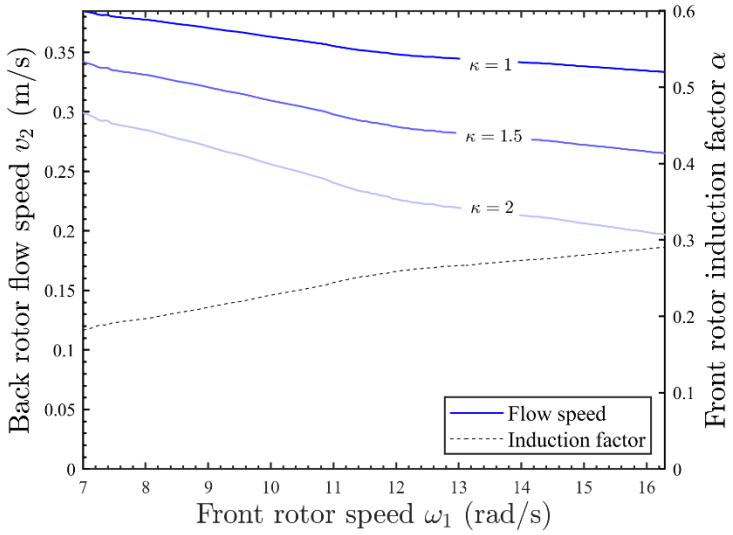

Figure 17. Axial induction factor and downstream flow speed for an ambient flow speed of 0.47 m/s, shown as a function of upstream rotor speed at several possibilities for wake expansion.

Once the upstream rotor torque τ_1 and downstream flow speed v_2 are determined, BEMT can be used to find the downstream rotor speed that minimizes the difference in torque magnitude between the rotors, at each upstream rotor speed. This minimization is also run using MATLAB's **`fmincon.m`** optimizer. The resulting downstream rotor speed for the 0.47 m/s case can be seen in Figure 18.

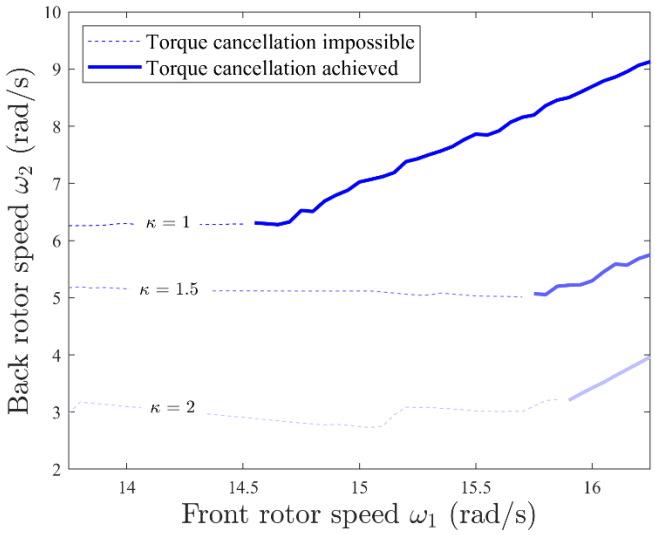

Figure 18. Downstream rotor speed solution that minimizes difference in rotor torque magnitude, for an ambient flow speed of 0.47 m/s. Dashed lines indicate no possible solution where the two rotors can generate torque of equal magnitude.

In this figure, it can be seen that there exists regions where torque cancellation is achieved, shown in solid lines, and regions where torque cancellation is impossible, shown in dashed lines. Because the flow to the downstream rotor is reduced from that of the upstream rotor, the maximum torque generated by the downstream rotor will be lower than that from the upstream rotor. At some values of ω_1, the associated upstream rotor torque is simply higher than anything the downstream rotor can produce, making it impossible to achieve equilibrium at that upstream rotor speed. This cancellation can be seen in Figure 19, where the minimum torque imbalance is nonzero for lower values of upstream rotor speed and higher upstream torque.

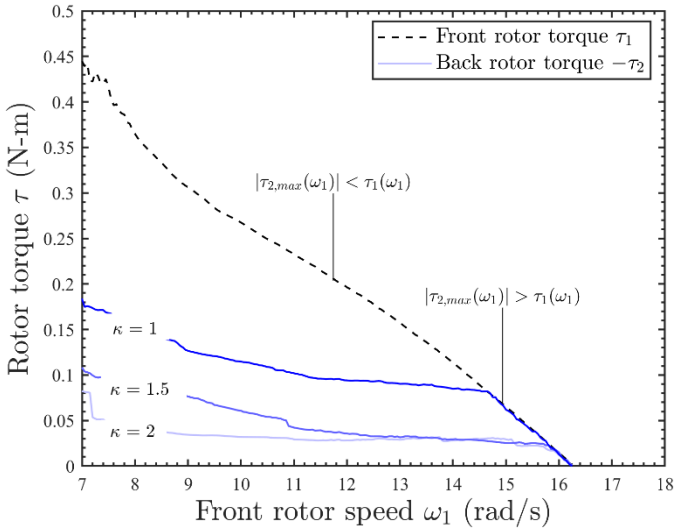

Figure 19. Downstream rotor torque associated with the rotor speeds in Figure 18, for the 0.47 m/s experimental case.

With the operation of both rotors known, the differential rotor speed can be used to determine the associated generator current, and by extension, required resistive load to achieve that current. The resistor load required for the 0.47 m/s case is plotted in Figure 20. Here, the inverse relationship between current and resistance, and by extension resistance and rotor speed outcome, can be clearly seen. Large resistors were chosen for the experiment to reduce the current and protect the onboard electronics, so the resulting predicted upstream rotor speeds for the experimental parameters varies by less than 1 rad/s. Additionally, the downstream wake development factor bears little effect on this required resistive load.

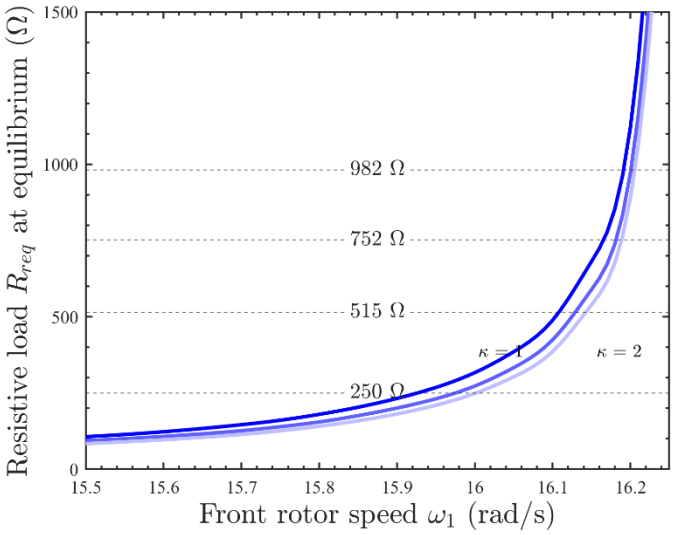

Figure 20. Resistor load required to achieve an operating point at a desired upstream rotor speed $\boldsymbol{\omega_1}$, for the 0.47 m/s case. Dashed lines indicate the resistors used in the tow-test experiment.

These analyses provide downstream rotor speed, turbine torque, and required resistive load as functions of upstream rotor speed. This implies that, given a wake expansion factor and ambient flow speed, any one of these four states can be used to determine the values of the other three. Since the experiment prescribed four different values for the onboard resistor, these values are used to predict the operating points of the rotor speeds and torque seen in the experiment.

6. Results

The predictions from the refined model are compared with the updated measurements from the experiment. For all test cases, upstream rotor speed, downstream rotor speed, and generator torque increase with flow speed as expected.

The operating points for the upstream rotor speed are shown in Figure 21 for all four tow speeds and all four prescribed resistor values.

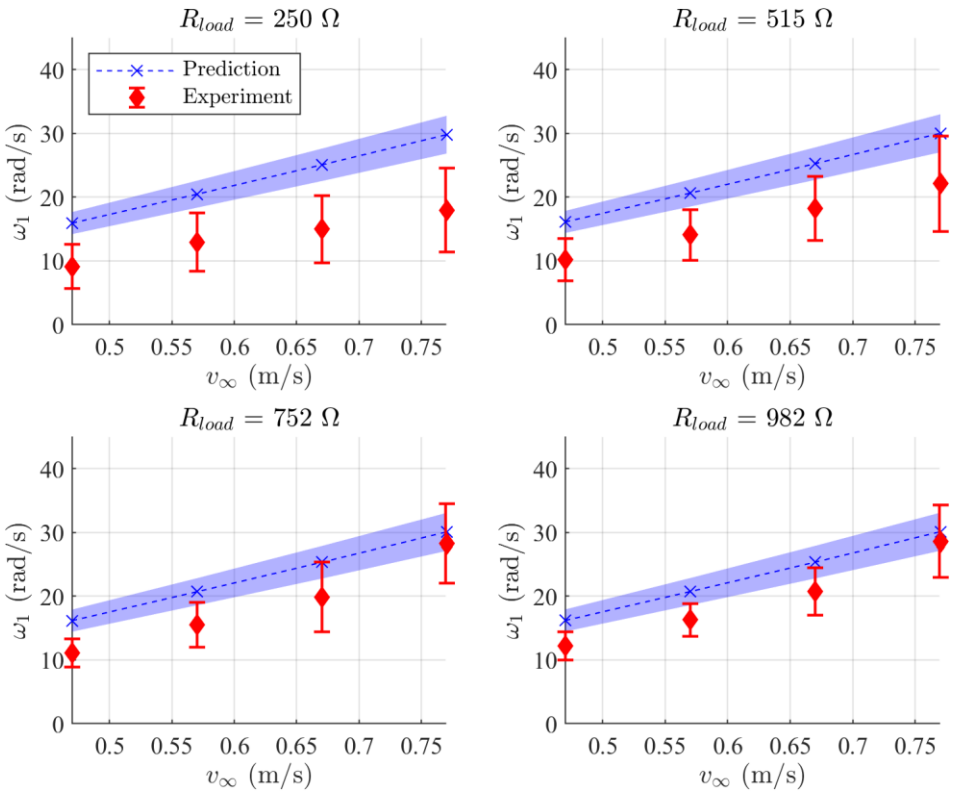

Figure 21. Model predictions vs. experimental results for steady-state upstream rotor speed. Prediction band indicates uncertainty in tow speed, error bars indicate one standard deviation of the measurements.

In all cases, the predicted front rotor speeds overestimated the speeds observed in the experiment, but with greater accuracy for higher resistive loads, and by extension, lower equilibrium torque. With the small torque magnitudes seen in Figure 19, the front rotor equilibrium speed predictions are near the predicted rotor speeds that generate zero net torque (ω_{max} as seen in Figure 16). Any overprediction of ω_1 may be due to mechanical losses, like friction between the upstream and downstream housing and in the tether's swivel bearings, or from the difficulty predicting low-Re behavior with XFOIL, as significant and sudden changes to the lift and drag curves occur across

the Re range present in the system during experimentation. The expected equilibrium front rotor speed exhibits negligible changes (<1%) across the range of possible degrees of wake expansion at the back rotor, due to the small values of torque seen in the experiment, suggesting a validation of the one-way assumption for rotor coupling.

Similarly, the predicted and measured operating points for the downstream rotor are compared for each experimental case in Figure 22.

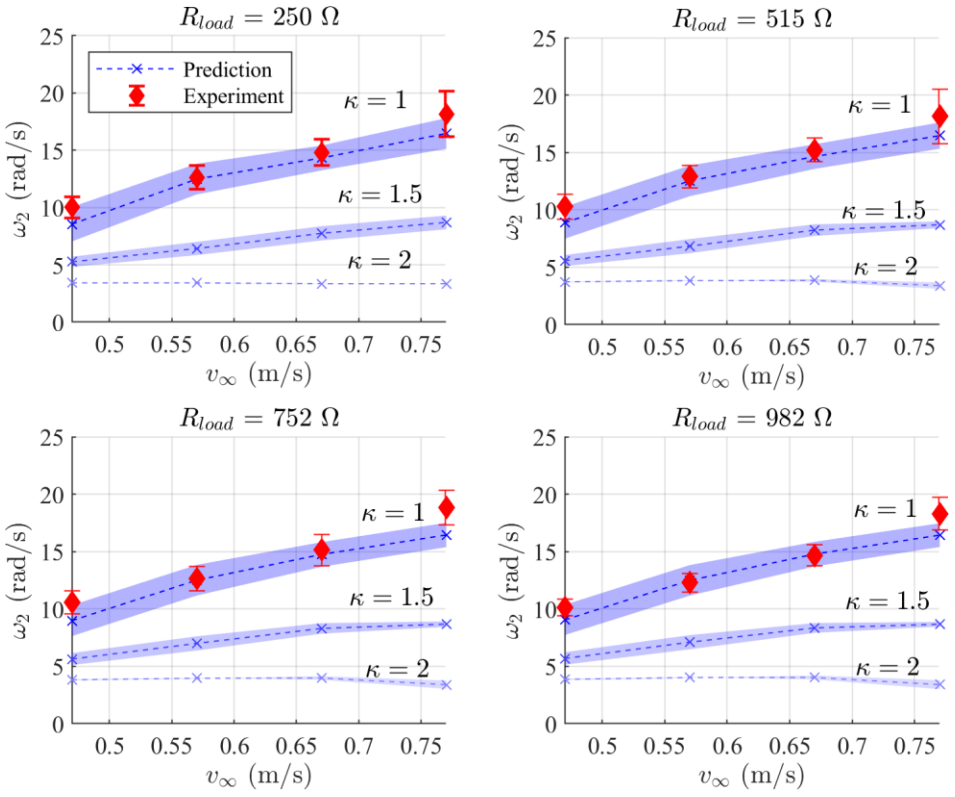

Figure 22. Model predictions vs. experimental results for steady-state downstream rotor speed. Prediction band indicates uncertainty in tow speed, error bars indicate one standard deviation of the measurements.

Although the wake behavior behind the upstream rotor is unknown, the downstream rotor speed is predicted across the entire range of possible levels of wake development. As expected, the back rotor speed is consistently lower than the associated front rotor speed due to the reduced flow regime from the wake of the front rotor. In each case, the back rotor equilibrium speed most closely matches with the behavior seen when $\kappa = 1$, suggesting the wake has little distance to advance before reaching the back rotor. Both rotor speed operating points from across the range of tested resistances remain tightly clumped together despite the highest resistance value being nearly four times that of the lowest value.

Finally, the predictions and measurements of steady-state turbine torque are shown below in Figure 23:

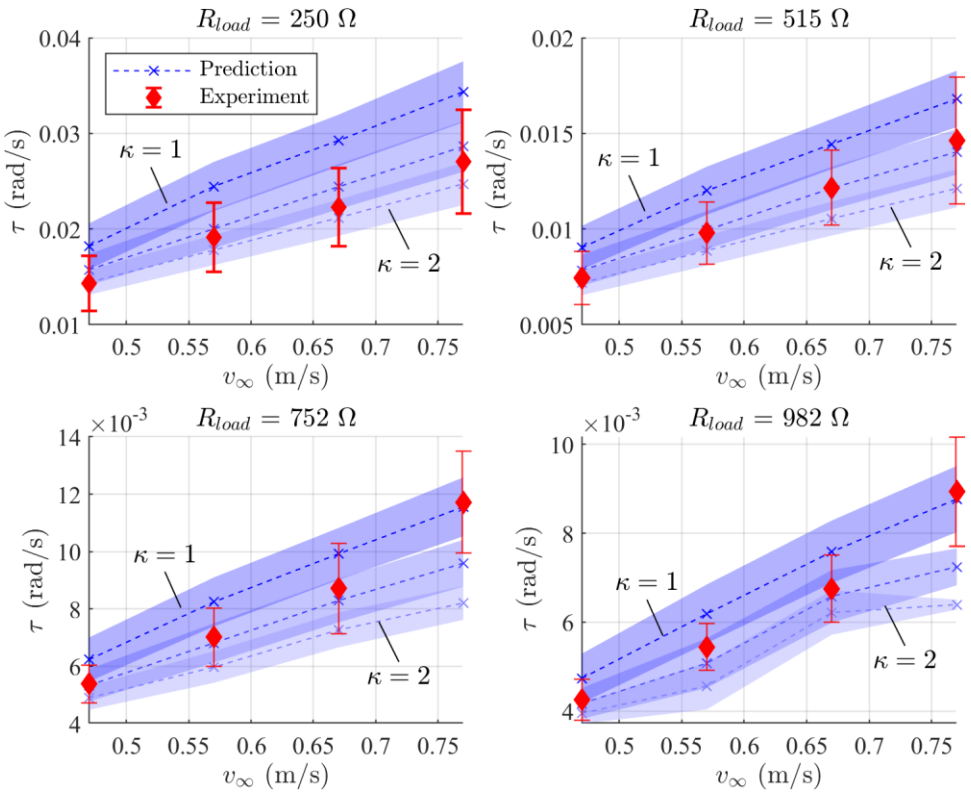

Figure 23. Model predictions vs. experimental results for steady-state downstream rotor speed. Prediction band indicates uncertainty in tow speed, error bars indicate one standard deviation of the measurements.

For all cases, the torque was measured to be nearly zero due to the high resistor values used in the experimental setup. The resistors were chosen to protect the electronics of the turbine, and Figure 20 suggests that the resistors would need to be an order of magnitude smaller to observe significant effects on the resulting torque. The predictions for the torque operating points also suggest a wake that is not fully developed at the back rotor, although the measurements agree more with a partially developed wake expansion of $\kappa = 1.5$.

7. Conclusions

A model is derived from the hypothesis that a single generator can be used to couple the upstream and downstream rotors of a coaxial turbine, and an experimental tow-test campaign utilizing a laboratory-scale prototype is run to observe physical behavior of the system. The results of the model prediction and the tow-test experimental campaign are compared, and similar trends are observed in both as freestream flow speed and resistive load were varied. These results also illustrate several findings: First, the steady-state rotor speeds are consistently higher for the upstream rotor than those of the downstream rotor due to the reduced downstream flow. Next, the resistive load had little effect on the steady-state rotor speeds, but an inverse relationship between resistive load and steady-state torque was observed. Finally, the state variables of upstream rotor speed, downstream rotor speed, and steady-state torque all display a linear relationship with freestream velocity.

While maximizing the power generated from a contra-rotating turbine is outside of the scope of this study, several remarks can be made from the analysis. Figure 19 illustrates the rotor speed envelope for a given turbine geometry and ambient flow. The lower bound of this envelope is the lowest rotor speed pair where torque cancellation is possible, and the upper bound of this envelope is the rotor speed pair where both rotors produce zero hydrodynamic torque. The turbine in this study used identical upstream and downstream rotors of uniform chord length, but a unique geometry for each rotor could potentially improve the torque produced in that speed envelope, as well as increasing the bounds of that envelope. The turbine in this study used a single resistor to select the operating point within that envelope, but a closed-loop control system could potentially be used to adjust the generator load to manipulate the turbine's operating point in real-time. Such

a control system could allow the turbine to seek the operating points of highest power generation in an ever-changing ocean current.

REFERENCES

[1] M. Tomczak and J. S. Godfrey, *Regional Oceanography: an Introduction.* Oxford, England: Pergamon, 1994.

[2] J. Clarke, G. Connor, A. Grant, C. Johnstone, and S. Ordonez-Sanchez, “Analysis of a single point tensioned mooring system for station keeping of a contra-rotating marine current turbine,” *IET Renewable Power Generation*, vol.4, no. 6, Nov. 2010, doi: 10.1049/iet-rpg.2009.0209.

[3] R. Metoyer, P. Chatterjee, K. Elfering, M. Bryant, K. Granlund and A. Mazzoleni, "Experimental analysis of dual coaxial turbines in skew," *Ocean Engineering*, vol. 215, Nov. 1, 2020: doi: 10.1016/j.oceaneng.2020.107877.

[4] R. Metoyer, P. Chatterjee, K. Elfering, M. Bryant, K. Granlund, and A. Mazzoleni, "Modeling, simulation, and equilibrium analysis of tethered coaxial dual-rotor ocean current turbines," *Energy Conversion and Management*, vol. 243, Sep. 1, 2021, doi: 10.1016/j.enconman.2021.113929.

[5] M. Nichols, “Torque Cancelling Equilibrium Operating Points of a Tethered Coaxial Dual-rotor Ocean Current Turbine,” M.S. thesis, Mech. Aero. Eng., NC State Univ., Raleigh., NC, 2021.

[6] A. R. Hambley, Electrical Engineering : Principles and Applications, 5 ed., Upper Saddle River, New Jersey: Pearson, 2011.

[7] R. Gasch and J. Twele, “Blade geometry according to Betz and Schmitz” in *Wind Power Plants: Fundamentals, Design, Construction and Operation*, 2nd ed., ch. 5, sec. 4, pp. 181-186. Accessed on: Apr. 29, 2023, [Online]. Available: https://link-springer-com.prox.lib.ncsu.edu/book/10.1007/978-3-642-22938-1

[8] M. O. L. Hansen, “The Classical Blade Element Momentum Method” in *Aerodynamics of Wind Turbines*, 2nd ed., Sterling, VA, USA, Earthscan, 2008, ch. 6, pp. 45-62.

[9] S. Schmitz, “Blade Element Momentum Theory (BEMT),” in *Aerodynamics of Wind Turbines: a Physical Basis for Analysis and Design*, Hoboken, NJ, USA: Wiley, 2020, ch. 3, sec. 1-5, pp. 51-78.

[10] J. C. Chapman, I. Masters, M. Togneri, J. A. C. Orme, "The Buhl correction factor applied to high induction conditions for tidal stream turbines," *Renewable Energy*, vol. 15, pp. 472-480, Jun. 15, 2013, doi: 10.1016/j.renene.2013.05.018

[11] J. Ledoux, S. Riffo, J. Salomon, “Analysis of the blade element momentum theory”, *SIAM Journal on Applied Mathematics*, vol. 81, no. 6, pp. 2596-2621, 2022, doi: 10.1137/20M133542X

[12] J. H. Jiménez, J. D. Hoyos, C. Echavarría, J. P. Alvarado, “Exhaustive analysis on aircraft propeller performance through a BEMT tool”, *Journal of Aeronautics, Astronautics and Aviation*, vol. 54, no. 1, pp. 13-24, 2022, doi: 10.6125/JoAAA.202203_54(1).02

[13] H. Snel, R. Houwink, J. Bosschers, W. J. Piers, G. J. W. van Bussel, and A. Bruining, “Sectional Prediction of 3D Effects for Stalled Flow on Rotating Blades and Comparison with Measurements,” in European Community Wind Energy Conference, Lubeck-Travemunde, Germany, Mar. 1993, pp. 395–399

[14] C. A. Lyon, A. P. Broeren, P. Giguère, A. Gopalarathnam, and M. S. Selig, “Summary of Low-Speed Airfoil Data,” UIUC, Champaign, IL, USA, 1997.